
PREMIXED TURBULENT FLAME STRUCTURES IN MODERATE AND INTENSE ISOTROPIC TURBULENCE

**R. K. CHENG*, I. G. SHEPHERD, B. BÉDAT,
AND L. TALBOT**

Environmental Energy Technologies Division,
Ernest Orlando Lawrence Berkeley National Laboratory,
Berkeley, California, USA

Several 2-D imaging techniques including planar laser induced fluorescence for OH (OH-PLIF) have been used to investigate premixed turbulent flame structures under moderate to intense isotropic turbulence. Unconditioned velocity statistics were measured by laser Doppler anemometry. The experiments used a low-swirl burner that produces high intensity near-isotropic turbulence. The goal is to gain better insights into the flame structures at high turbulence and to test and verify the concept of the “distributed reaction zones” regime. Four methane/air flames ($\phi = 0.7$) have been studied with $0.5 < u' < 2.2$ m/s. A linear correlation for the flame speed, S_f , is found: $S_f/S_L = 2.12(u'/S_L) + 1$. Sets of 200 OH-PLIF images obtained for each flame clearly show that flame wrinkling is a random process. The probability of the flame having very small wrinkles is relatively low. This strongly suggests that the penetration of small intense eddies into the flame sheet to generate a “distributed reaction zone” is statistically an extremely rare event. The OH-PLIF images were processed to determine statistical properties of the mean flame curvatures and flame lengths

Received 15 March 1999; accepted 30 July 2001.

This work was supported by the Director, Office of Energy Research, Office of Basic Energy Sciences, Chemical Sciences Division of the U.S. Department of Energy under Contract No. DE-AC03-76SF00098. The authors would like to acknowledge Mr. Gary Hubbard for writing the computer controlled and data reduction software and Mr. Scott Fable for assisting with image processing.

This paper was presented at a Joint U.S.-French Workshop on Premixed Turbulent Flames, Hilton Head, SC, 6–7 December 1996.

*Address correspondence to RKCheng@lbl.gov

for comparison with turbulence intensity and turbulent length scales. The results show that the increase in turbulent kinetic energy generates larger mean curvatures of the flame fronts, and a linear increase in the flame surface area ratio estimated from the mean flame length measurement.

Keywords: premixed turbulent flame, experimental, laser

INTRODUCTION

The classification of premixed turbulent flames originates with Damköhler (Damköhler, 1940) who defined turbulent burning velocity expressions for small-scale and large-scale turbulence regimes. His concept has been a useful guide for experimentalists and theoreticians, and has since been elaborated to include several different flame regimes. These regimes are usually expressed on phase diagrams of nondimensional mixture and turbulence parameters. Figure 1 shows a version based on u'/S_L and l_x/d_L that is often referred to as the Borghi-Barrère diagram (Borghi, 1985). Another version uses the turbulent Reynolds number, Re_t , and the Damköhler number, Da as the variables. The important

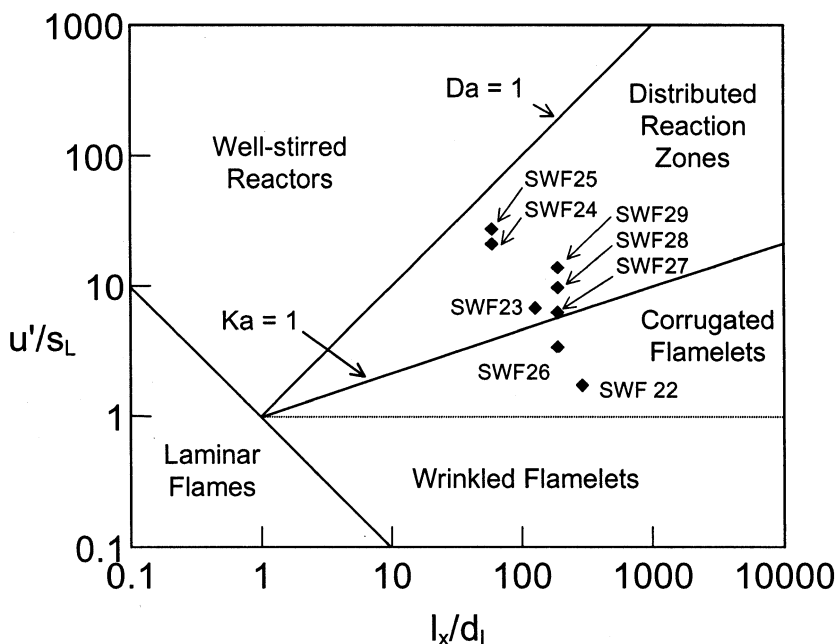


Figure 1. Regime diagram for premixed turbulent flames.

underlying assumption of the phase diagram is that the scaling laws for nonshear, fully developed isotropic turbulence are applicable so that $Da = (l_t/d_L) (u'/s_L)^{-1}$ and $Ka = (u'/s_L)^{3/2} (l_x/d_L)^{-1/2} = (d_L/l_k)^2$ (Peters, 1986). The reaction zone thickness, d_L is defined by the Klimov criterion $d_L S_L = v$. The $Ka = 1$ boundary, generally known as the Klimov-Williams criterion (Peters, 1986), separates the regimes of wrinkled laminar flames (i.e., thin reaction zones) from flames with thicker distributed reaction zones. There is much interest in verifying experimentally the changes in flame structures as predicted by the Klimov-Williams criterion because the operating conditions of many practical systems span the criterion boundary and theoretical treatments of the two flame regimes can be quite different.

Previous experiments to verify the Klimov-Williams criterion have mostly been inconclusive (Furukawa, Harada, & Hirano, 1990; Yoshida, Narisawa, & Tsuji, 1992). Due to the difficulties in generating intense isotropic turbulence in laboratory experiments, these studies have used flames with high shear turbulence. Moreover, the diagnostics (line-of-sight schlieren imaging, Yoshida et al. and ion-probe, Furukawa et al.) are, at best, indirect means for probing the structures of the flame fronts. In a recent investigation (Bedat and Cheng, 1995), a low-swirl burner was used that can stabilize lean premixed turbulent flames in intense isotropic turbulence of up to 20 percent (Fig. 2). The burner produces a turbulent flow field that conforms to the turbulence scaling laws implicit in the phase diagrams. Laser Doppler anemometry and Rayleigh scattering techniques were used to measure velocity and scalar statistics. The data show that, even under intense isotropic turbulence with $Ka = 18.8$, the probability density functions (pdf) of the Rayleigh scattering signals are distinctly bi-modal and not significantly different from those measured in flames at $Ka < 1$. These data seem to support recent numerical and theoretical results (Poinso et al., 1990; Jarosinski, 1984), suggesting that flamelets are more resilient to penetration by small eddies than is prescribed by the Klimov-Williams criterion.

To gain better insight into the turbulent flame structures at high turbulence, this study uses a planar laser induced fluorescence (PLIF) technique for OH radicals. OH is a convenient marker of the reaction zone because its concentration increases sharply at the leading edge of the flame (i.e., the edge that faces the cold reactants). Significant broadening of the reaction zone, as postulated for flames within the distributed reaction zone, should weaken the sharp increase in OH concentrations.

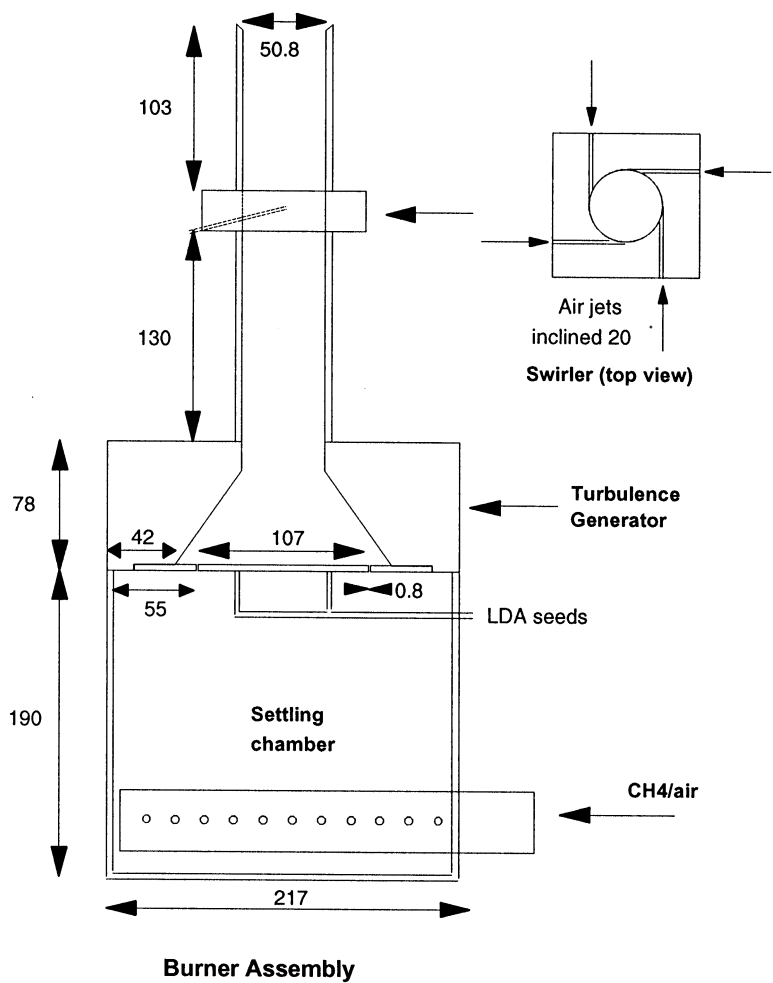


Figure 2. Schematics of the low-swirl burner with a circular slot turbulence generator.

Due to the strong fluorescence signal, this imaging method offers a relatively high signal-to-noise ratio and a larger field of view than other comparable 2-D sheet imaging methods. It should therefore provide the data necessary to improve our understanding of flame structures and to determine other flame properties such as flame curvatures and flame lengths. We also used schlieren and tomography to observe overall flame brush characteristics and to demonstrate why these techniques are not

adequate for verifying the Klimov-Williams criterion. Other diagnostics included two component LDA for velocity statistics and Mie scattering from oil aerosol technique for flame crossing frequencies and mean reaction progress variable.

EXPERIMENTAL APPARATUS

The low-swirl burner is shown schematically in Figure 2 (Bedat and Cheng, 1995). It consists of a settling chamber, a turbulence generator, and a cylindrical burner tube fitted with an air swirler section. The turbulence generator is a circular adaptation of the linear slot design of Videto and Santavicca (1991). It has a linearly convergent nozzle (contraction ratio = 7) fitted on top of a bottom plate. A 0.8 mm wide, 107 mm diameter axisymmetric slot cut into the bottom plate allows the CH_4 /air mixture to enter from the settling chamber. As the highly sheared flow issuing from the slot impacts on the inclined wall of the convergent nozzle wall, large vortical structures are broken down to finer isotropic turbulence eddies. Pressure drop across the turbulence generator was calibrated to the flow rate and then used as a means to monitor the flow.

Flame stabilization was achieved by the low-swirl method (Chan, Lau, Chin, & Cheng, 1992; Cheng, 1995; Bedat & Cheng, 1995). The air swirler has four 2.5 mm diameter tangential air jets tilted upwards by 20° . The jets are individually adjustable and their total flow rate is monitored by a rotameter. The 103 mm long burner tube section on top of the air swirler allows the swirl air to interact with the main flow. These small air jets induce very weak angular momentum and so only influence the outer flow region. As the premixture exits the tube, the annular swirl generates a divergent flow instead of forming a recirculation zone. The exit rim is tapered at 45° to guide the flow divergence. This divergence allows the premixed turbulent flame to settle at the position where the local flow velocity is equal to the flame speed. The swirl number, S , given by Claypole and Syred (1980) also applies to the low-swirl burner. However, the values here are much lower, typically from $0.02 < S < 0.1$ compared to $S > 0.6$ in a conventional high-swirl burner. The flame generated by the low-swirl burners is freely propagating. As the bowl-shaped flame brush propagates normal to the approaching flow, it receives more uniform turbulence than oblique flame or shear flame configurations.

EXPERIMENTAL CONDITIONS

Table 1 shows the experimental conditions of the four methane/air flames used in this study (SWF26 to WSF29). Also shown are those reported studied by Bedat and Cheng (1995)* (SWF22 to SWF25). The equivalence ratios of these four new flames are fixed at $\phi = 0.7$ so that they have the same laminar flame reference. Their flow rates, Q , vary from 5 liter/sec to 20 liter/sec corresponding to reference velocities, U_∞ , of 2.5 to 10 m/s. These flames were all stabilized with $S = 0.1$. A unique feature of the turbulence produced by the slot generator is that the integral length scale, l_x , is independent of U_∞ . Therefore, SWF26–29 have the same l_x/d_L ratio and appear on a vertical axis on the Borghi-Barrère diagram (Figure 1).

The values of s_L listed in Table 1 are obtained by fitting the experimental measurements of Tseng, Ismail, and Faeth (1993) for non-stationary laminar premixed hydrocarbon flames with $\phi \geq 0.6$. Reliable s_L data for lean premixed methane flame are important to our study because the values of Da and Ka are very sensitive to s_L . This is especially critical for $\phi < 0.7$ where s_L becomes very small (≈ 0.1 m/s) and the scatter in theoretically calculated s_L data can be as high as 200 percent. For example, the value of $s_L = 0.15$ m/s at $\phi = 0.6$ used in Bedat and Cheng (1995) was based on extrapolating the data of Taylor (1991). This value is almost 2.4 times higher than the measured value of Tseng et al. are. The large uncertainties in s_L is the primary reason for not setting the experimental conditions closer to $\phi = 0.6$ (e.g. SWF25) even though these conditions are further within the distributed reaction

Table 1. Experimental conditions and relevant parameters

	ϕ	S_l	U	u'	l_x	d_l	Re	Da	Ka	u'/S_L	S_f/S_L
SWF22	0.80	0.304	2	0.52	0.015	5.12E-05	500	139.9	0.13	1.71	4.6
SWF23	0.65	0.132	3	0.89	0.015	0.000118	856	15.5	1.55	6.72	14.0
SWF24	0.60	0.062	5	1.3	0.015	0.000253	1250	2.3	12.60	21.10	46.4
SWF25	0.60	0.062	7	1.7	0.015	0.000253	1635	1.8	18.84	27.60	58.9
SWF26	0.70	0.196	2.5	0.5	0.015	7.94E-05	481	60.6	0.29	2.55	7.6
SWF27	0.70	0.196	5	1.22	0.015	7.94E-05	1173	24.8	1.13	6.21	15.3
SWF28	0.70	0.196	7.5	1.9	0.015	7.94E-05	1827	15.9	2.19	9.67	21.4
SWF29	0.70	0.196	10	2.2	0.015	7.94E-05	2115	13.7	2.73	11.22	28.0

zone regime. Furthermore, Tseng et al.'s measurements at $\phi = 0.7$ have been verified with our measurements in a buoyancy stabilized stationary flame (Bedat and Cheng, 1996).

DIAGNOSTICS

The two-component LDA is a four-intersecting-beam frequency-shifted system consisting of two TSI frequency counters (Cheng, 1995). It measures the axial velocity component, U , and the radial component, V , with a differential shifting frequency of 5 MHz for both components. The circumferential velocity component, W , was not measured because this component is zero in the vicinity of the centerline. Unconditioned velocity statistics were obtained by seeding the fuel/air flow with aluminum oxide particles of 0.3 μm diameter. Mean velocities, fluctuating velocities, and Reynolds stresses are deduced from 2048 validated velocity pairs obtained using a 10 μs coincidence criterion. The velocity spectra for the longitudinal velocity fluctuations, u' , were measured by sampling the analog counter output at a fixed rate of 10 KHz. This procedure is identical to that described previously (Cheng).

To determine the time and length scales of the scalar fluctuations, the Mie scattering from oil droplet method (MSOD) (Cheng, 1995) was used to measure flame crossing frequencies, f and mean reaction progress variable, \bar{c} . The MSOD optics are integrated into the LDA system. A photomultiplier arranged perpendicularly to the beam direction collected Mie scattering intensities at the beam waist of the two 488 nm intersecting beams. As the oil aerosol in the premixture burns and evaporates at the flame front, the Mie signal in a turbulent flame resembles that of a random telegraph signal. Using an on-line, two-threshold criterion, the mean transit times for the reactants and products from this signal are used to compute f and \bar{c} according to previously established procedures.

Three imaging techniques have been used in this study: laser schlieren, tomography, and PLIF. Laser schlieren is the most straightforward. Its optics consist of a pair of 15 cm diameter, 1.2 m focal-length spherical mirrors, a short focal-length expanding lens, and a 0.3 mW Helium-Neon laser source arranged in a standard "Z" configuration. The schlieren stop is an opaque circular spot etched on a microscope slide. This method produces reverse-field schlieren images with the flames shown as bright regions against a dark background. The sensitivity of the schlieren system is determined by the size of the opaque spot. Different schlieren stop radii

were tested to produce “clean” schlieren images. We found that the conventional approach (i.e., maximize system sensitivity by using the smallest allowable schlieren stop) produced images that contain contributions from surround heat currents. Consequently, clarity of the images is compromised, and interpretation becomes quite impossible. This optimization process for applying schlieren to flames is usually not discussed in other investigations.

The tomographic technique is a 2-D imaging version of MSOD. Illuminating the aerosol with a laser sheet and capturing the Mie scattering by a camera produces an image that delineates the flame boundaries separating the hot products from the cold reactants. The tomography systems employ a Spectra-Physics Quanta Ray DCR-2A Nd:YAG laser. The strong Mie scattering intensities allow a sufficiently large field of view to capture the entire turbulent flame brush. The laser has a pulse energy of 400 mJ (@ 532 nm) with a pulse width of 8 ns. A simple cylindrical lens shaped the laser beam into a sheet of 75 mm in height and approximately 200 μm in thickness. An intensified Xybion CCD camera with a standard zoom lens captures a field of view up to 120 mm \times 120 mm.

For PLIF, the second harmonic of the Nd:Yag laser is used to pump a Spectra Physics Quanta Ray dye laser with Rhodamine 590 dye (Figure 3). A frequency doubling crystal for the dye laser output

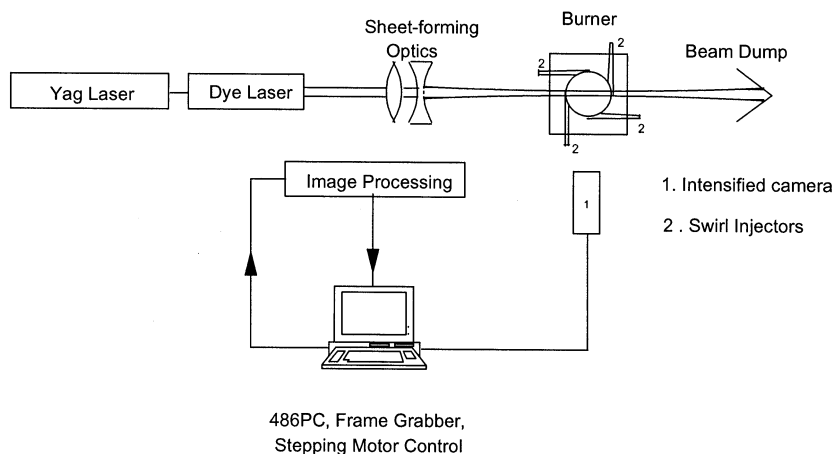


Figure 3. Schematics of the OH-PLIF system.

generates an ultra violet (UV) beam that is tuned to the $P_1(2)$ absorption transition (282.58 nm) of the OH (1,0) band of the $A^2\Sigma^+ \leftarrow X^2\Pi$ system. OH fluorescence at 306.4 nm is detected by the use of band pass filters placed in front of the Xybion camera. This system is capable of producing tunable output at up to 50 mJ/pulse. For PLIF, the laser beam is shaped into a thin (less than 200 nm) vertical sheet 30 mm high to optimize the signal to noise ratio. The PLIF system affords a field of view of 40 mm by 40 mm at a resolution of 0.08 mm/pixels. This is sufficient to capture the largest relevant flame wrinkles and to span most of the turbulent flame brush.

The tomography and PLIF systems share many electronic components and data acquisition software. The laser pulse rate of 10 Hz provides the synchronization signal for the CCD camera and a six-buffer video PC card. The data acquisition software can also record and store the images continuously at approximately 1 Hz. For this study, we obtained 200 OH-PLIF images for each flame. To correct for variations in the laser intensity across the beam (i.e., the vertical direction on the PLIF images), a set of lean laminar v-flame images was obtained. In the narrow products region between the two branches of the very oblique v-flames, the concentrations of OH do not decay rapidly and provide a convenient means of showing the beam profile. From the laminar flame images, we concluded that a Gaussian distribution would be sufficient to correct for the variation in beam intensity. In addition, OH-PLIF images of laminar conical flames at $\phi = 0.7$ were also obtained. These results provide a baseline OH fluorescence intensity profile of a laminar flame front for comparison with those measured across the reaction zone of the turbulent flames.

RESULTS

Point Statistics

Figure 4 shows the nonreacting centerline profiles for SWF26–29. All the U profiles have a characteristic linear deceleration with increasing x . The mean aerodynamic stretch rates, a_b , deduced from the slopes are 70, 115, 198, and 263 sec^{-1} , respectively, for SWF26–29. These stretch rates are comparable to those generated in stagnating flows. The linear decelerations continue until U reaches zero at $30 < x < 40$ mm. Beyond this position, all profiles level off to about $-1 < U < 0$ m/s. This feature of the mean profiles indicates an absence of strong recirculation and

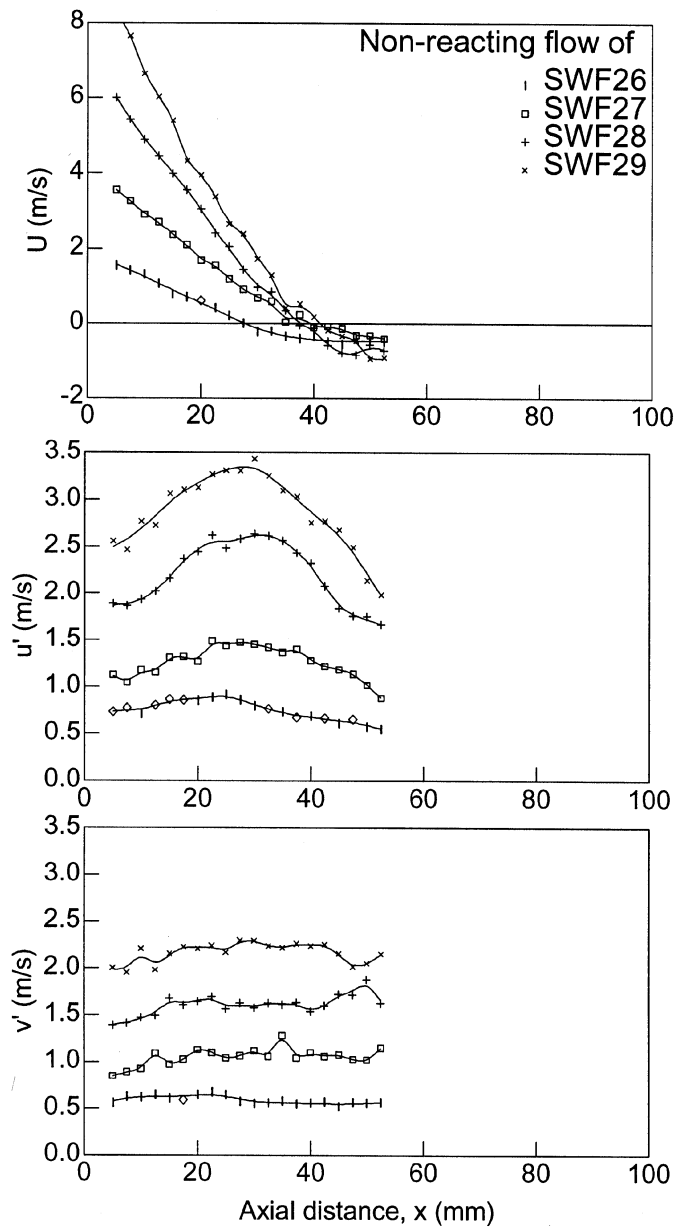


Figure 4. Nonreacting mean and rms velocity.

is a characteristic of isothermal flow generated by low swirl. The rms velocities at the burner exit (Figure 4) show that the turbulence level produced by the round-slot turbulence generator is directly proportional to the flow rate. This turbulence, however, is slightly anisotropic with v' about 20 percent lower than u' . The extent of this isotropy is about the same as that produced by a grid or perforated plate. Further downstream, the v' profiles remain relatively flat while the u' profiles of SWF28 and SWF29 increase to show local maxima.

The unconditioned reacting mean velocity profiles of SWF26–29 in Figure 5 also have an initial linear decelerating region immediately downstream of the burner exit. This is followed by a relatively flat or slightly decelerating region within the flame brush. The point of inflection (e.g. near $x = 20$ mm for SWF29) serves as a convenient marker for the leading edge of the turbulent flame brush. The presence of the flame also changes a_b in the reactants to 55, 82, 203, and 191 sec^{-1} . Without observable velocity increases, the U profiles demonstrate that combustion generated flow acceleration is insignificant. This feature is consistent with the u' and v' profiles that have no local peaks. This implies that the differences between the conditional mean velocities in the reactants and in the products are small.

A lack of distinct features in these velocity profiles demonstrates again that the flow field characteristics of premixed turbulent flames are greatly dependent on the incident turbulence intensity, heat release ratio τ , and the flame configuration. As discussed by Cheng (1995), counter gradient transport of scalar and turbulence is observed only in low and moderate turbulence with high τ values. It is caused by intermittent sampling of the higher conditioned velocities in the products and the lower conditioned velocities in the reactants (i.e., relative velocity $\Delta U > 0$). The contributions to the unconditioned rms velocities is also directly proportional to ΔU . As the magnitude of ΔU is prescribed by the product of S_L and $\tau - 1$, its effect is diminished when the mean (a_b) and turbulent (a_t) stretch rates are high. Cheng proposed an indicator parameter K_t to estimate the relative effect of these stretch rates on ΔU and demonstrated that flames with $K_t \geq 100 \text{ m}^{-1}$ do not exhibit counter gradient transport characteristics. For SWF26–29, the values of K_t are 95, 150, 336, and 358 m^{-1} , respectively. The mean and rms velocity profiles shown in Figure 4 further support this qualitative interpretation.

In accord with our previous definition (Bedat and Cheng, 1995), the flame speed s_t is defined by the axial velocity at $\bar{c} = 0.05$. Figure 6 shows

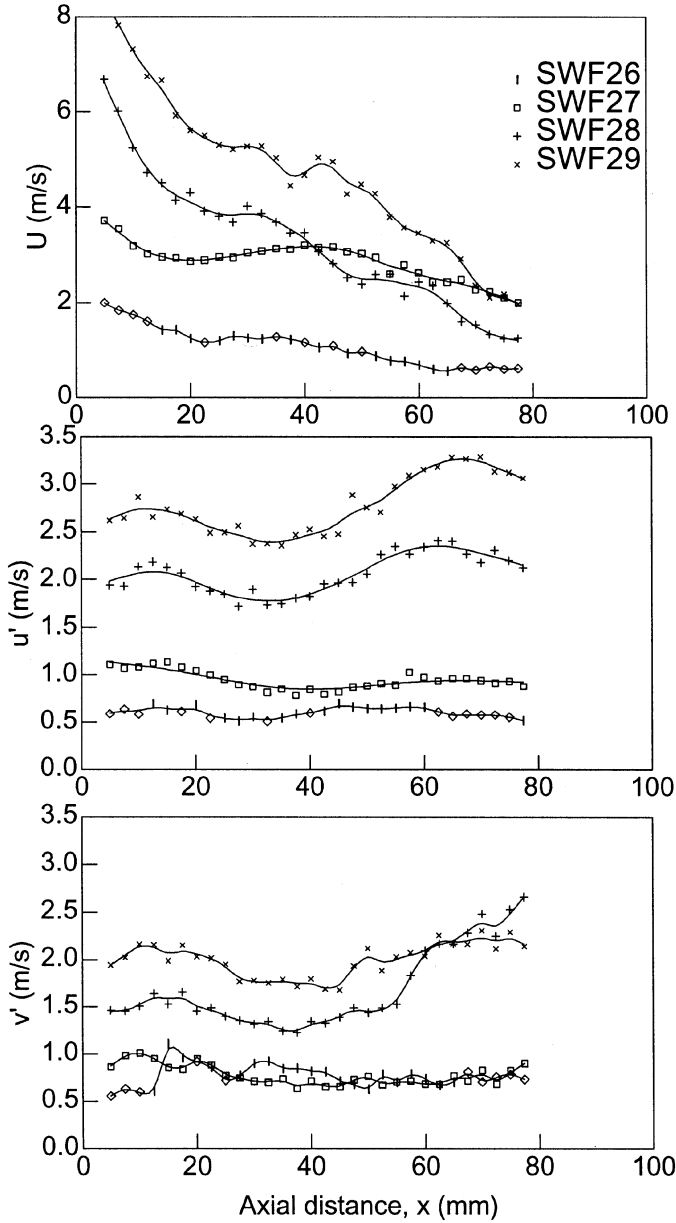


Figure 5. Reacting mean and rms velocity.

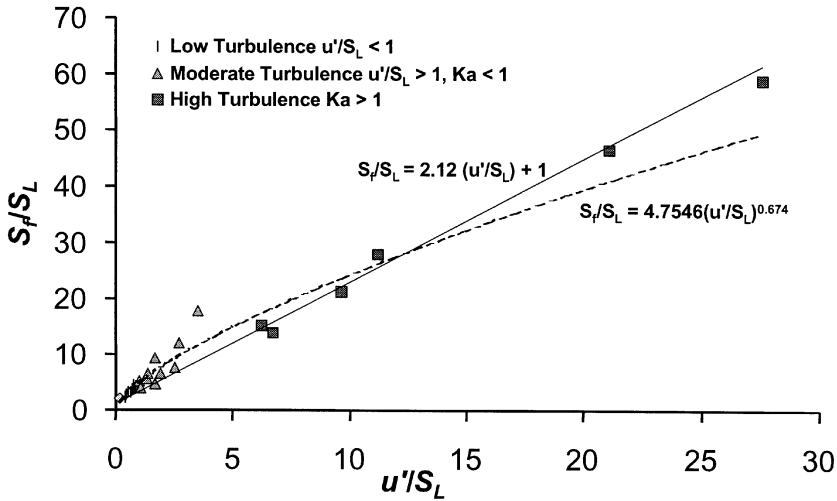


Figure 6. Correlation of flame speed obtained in two different low-swirl burners for methane-air and ethylene-air mixtures.

the flame speeds of SWF26–29 together with those measured by Cheng (1995) (SWF1–21), and by Bedat and Cheng (1995) (SWF22–25). Here, the set of data SWF1–29 is re-normalized by the laminar flame speeds obtained by Tseng. The most noticeable consequence of this new plot is that the leanest flames (SWF24 and 25) have substantially higher values of S_f/S_L and u'/S_L than reported previously (Bedat and Cheng). These changes, however, do not alter the linear relationship shown between S_f and u' . The least square fit for the entire set of S_f data measured in two versions of the low swirl burner (SWF1–9 for ethylene/air, Cheng and SWF10–SWF29 for methane/air) has a slope of 2.12. This is consistent with the theoretical prediction of $S_f \approx 2.1u'$ by Pope and Anand (1984) for flamelets and distributed reaction zones. This linear trend, observed even at large values of u'/S_L is a significant departure from the nonlinear trend found for nonstationary propagating flames (Bradley, 1992). Deviation from the linear flame speed correlation is commonly known as the “bending effect” of S_f and has also been reported for stationary flames with small values of $u'/S_L < 3$ (Bray, 1990). To investigate whether our data set supports this nonlinearity, also plotted in Figure 4 is a power function fit of the data. Though the function has an exponent of 0.67 that is close to the value of 0.7 obtained from analysis (Williams,

1985), it is obvious that the evidence for the bending of S_f for flame stabilized in the low swirl burner is not compelling.

Figure 7 shows profiles of \bar{c} measured in SWF26–29. To determine their self-similarity, the origins of these profiles have been shifted to the x positions at $\bar{c} = 0.5$. The shape of the \bar{c} profiles is identical to those observed in other premixed turbulent flames. Figure 5 also shows that the flame thicknesses do not vary significantly despite a substantial change in flow rates and turbulence intensities. By fitting the profiles with an expression of the form $1/[\exp(-4x/D_f)]$, a flame brush thickness, D_f , can be defined. This definition is essentially the steepest slope method and gives D_f for SWF26–29 of 34, 26, 28, and 31 mm, respectively. These values are approximately twice the integral turbulence length scale of $l_x = 15$ mm.

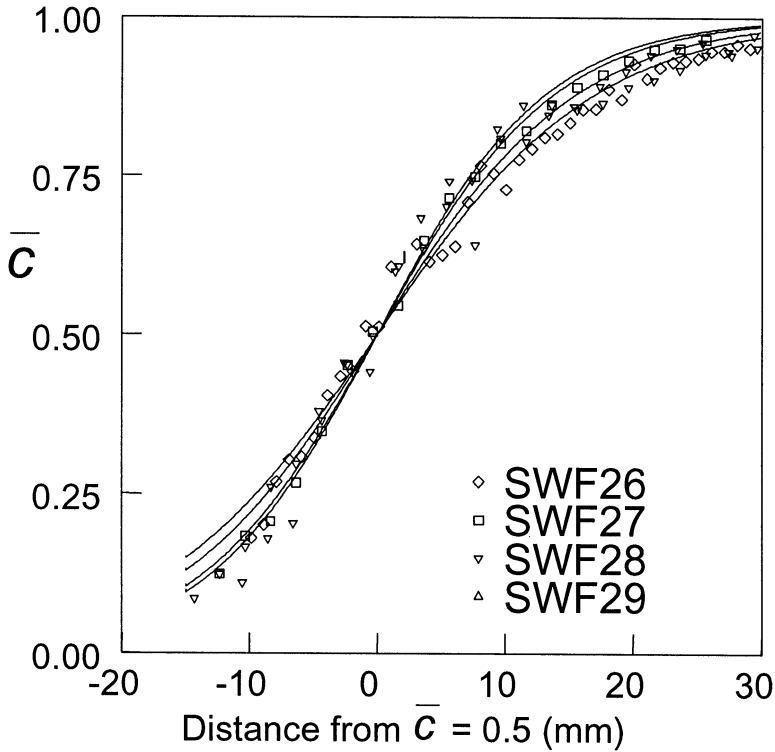


Figure 7. Mean \bar{c} profiles to compare the turbulent flame brush thicknesses.

Profiles of the flame crossing frequency, f , normalized by the integral, $\int_0^1 f(\bar{c}) d\bar{c}$, are shown in Figure 8. This normalization method is convenient for a direct comparison with the idealized symmetric distribution $\bar{c}(1 - \bar{c})$. The peak flame crossing frequencies, f_{\max} , for SWF26–29 are 102, 188, 216, and 380, respectively, and show a general increasing trend with turbulence intensity. Due to the high turbulence intensities and the relatively low mean velocity, Taylor's hypothesis would not be reliable for inferring the length scales from the values of f . However, the shapes of the f profiles offer some interesting insight into features of the flame wrinkles. All the f profiles obtained in different flame configurations tend to skew toward $\bar{c} > 0.5$. This skewness has been attributed to the formation of flame cusps. Here, only the SWF26 profile shows such skewness and the profiles for flames SWF27–29 are less skewed, indicating that the formation of flame cusps is not as important

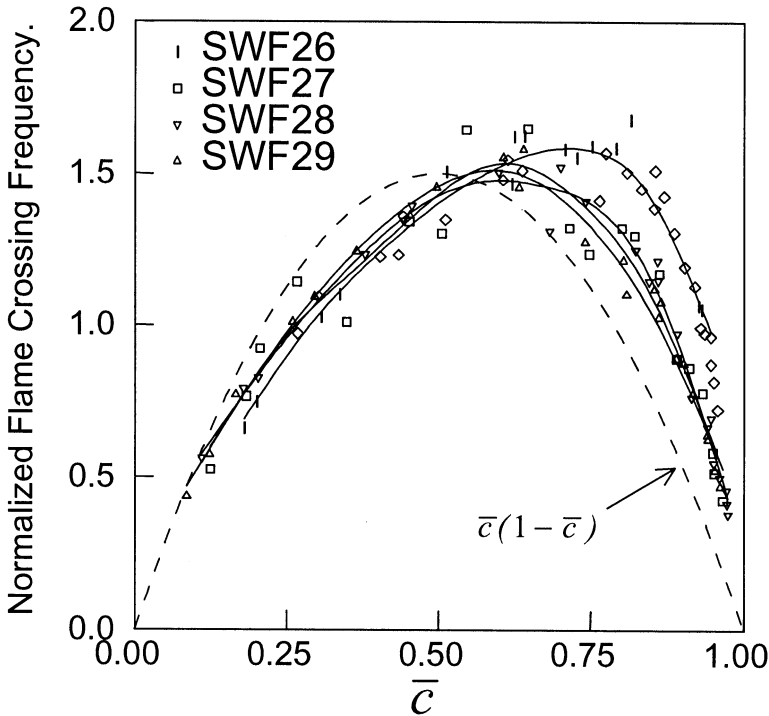


Figure 8. Normalized flame crossing frequency compared to the $\bar{c}(1 - \bar{c})$ distribution.

in higher turbulence cases. This observation is confirmed by our PLIF results (to be discussed later) and is consistent with recent theoretical analysis by Peters (1998). The change in cusping behavior can be explained by the diminishing effects of normal flame front propagation mechanism that generates flame cusps. It has been identified by Peters as a sink term, kinematic restoration, in the flame surface area equation that counteracts the wrinkling effects of turbulence. Kinematic restoration is proportional to the laminar flame speed S_L , and is therefore insignificant compared to the turbulence for large values of u'/S_L .

2-D Imaging

As discussed earlier, the motivation for applying schlieren and tomography is to gain an overview of the flow field behavior and to demonstrate why they are not sufficient to show detailed flame structures. Figure 9 compares the schlieren and tomographic images for SWF 14 (within the wrinkle flamelet regime with $\phi = 0.8$, $u'/S_L = 0.92$) and SWF25 (well within the distributed reaction zone regime). Schlieren is a line-of-sight integration method that does not offer spatial resolution in the direction normal to the image plane. Flame fronts or heat currents along the beam path overlap on the images. The surrounding heat currents can contribute substantial background noise to the schlieren image. If the sensitivity of the schlieren systems is not tuned to avoid capturing these heat currents, contributions from flame fronts cannot be distinguished. As seen here, even with our optical system optimized, the only useful information gained from the schlieren images other than the overall flame size is that SWF25 has the finer flame wrinkle scales. Further attempts to interpret the shapes and thickness of the flame front structure would seem to be purely speculative.

The tomographic method provides a spatially resolved cross-sectional view of the flame and is a more reliable means than schlieren for investigating the flame wrinkle structures. The reactants stream appears bright due to Mie scattering from the aerosol droplets. As the aerosol burns and evaporates at the flame, the sharp boundary between the bright and dark regions outlines the flame fronts. The tomographic images of Figure 9 show that SWF14 has large wrinkles and sharp flame cusps typical of those observed in flames within the flamelet regime. In comparison, SWF25 has finer wrinkles, appears more convoluted and does not have sharp flame cusps. The formation of “pockets” in the reactants

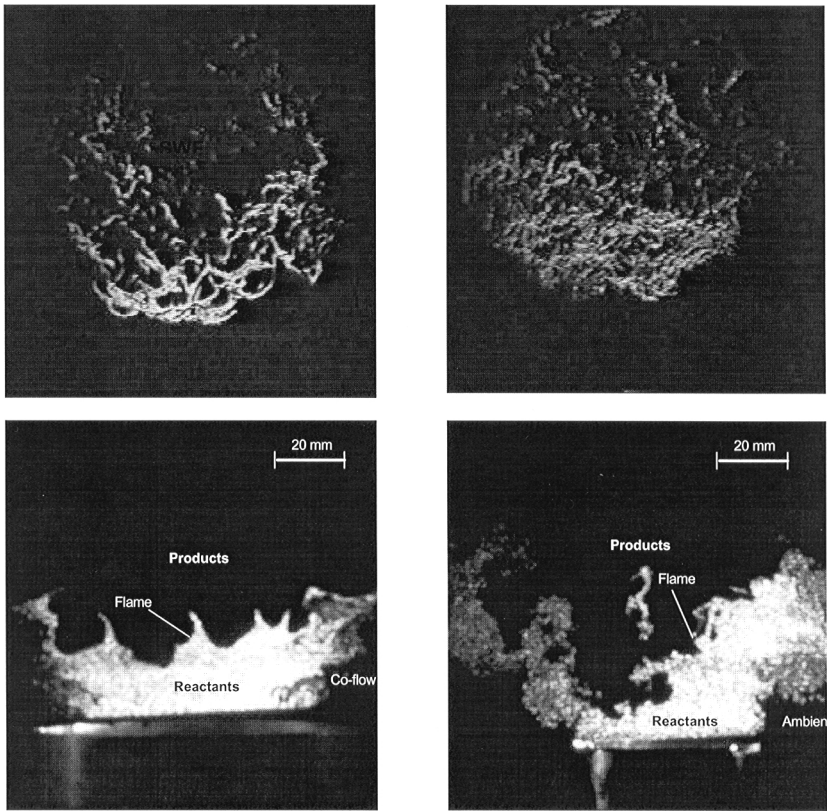


Figure 9. Comparison of schlieren (top) and tomographic (bottom) obtained for SWF14 and SWF25.

or in the products is also apparent. Closer inspection of the tomographic record, however, reveals that the droplet density of the aerosol limits the capability of this method to resolve the small flame wrinkle structures that exist at high turbulence levels. Though this is a limitation of the technique, the large field of view afforded by tomography was very useful for surveying the overall features of the entire flow field. For example, flow divergence induced by low-swirl is illustrated by the widening reactants stream. The mixing layer between the reactants and ambient air is also seen to the sides of the flame. It is also useful to learn from the tomographic study that the flame can sometimes be asymmetric (e.g. Figure 7, SWF25) and shifted to one side. Though this asymmetry

is random and does not appear in the mean properties, this behavior explains why the PLIF systems, with a smaller field of view centered on the axis, can occasionally not capture the flame.

Four sets of OH-PLIF images for SWF26–29 are compared in Figure 10. The OH-PLIF images are essentially reverses of tomographic images: The products region appears bright. To illustrate the changes in flame wrinkle structures from one image to the next, Figure 10 shows three columns representing different degrees of flame wrinkling. Shown to the right are the corresponding \bar{c} maps of the flame brushes deduced from the 200 images. These \bar{c} maps illustrate that the 40×40 mm field of view of the OH-PLIF optical system captures most of the flame brush

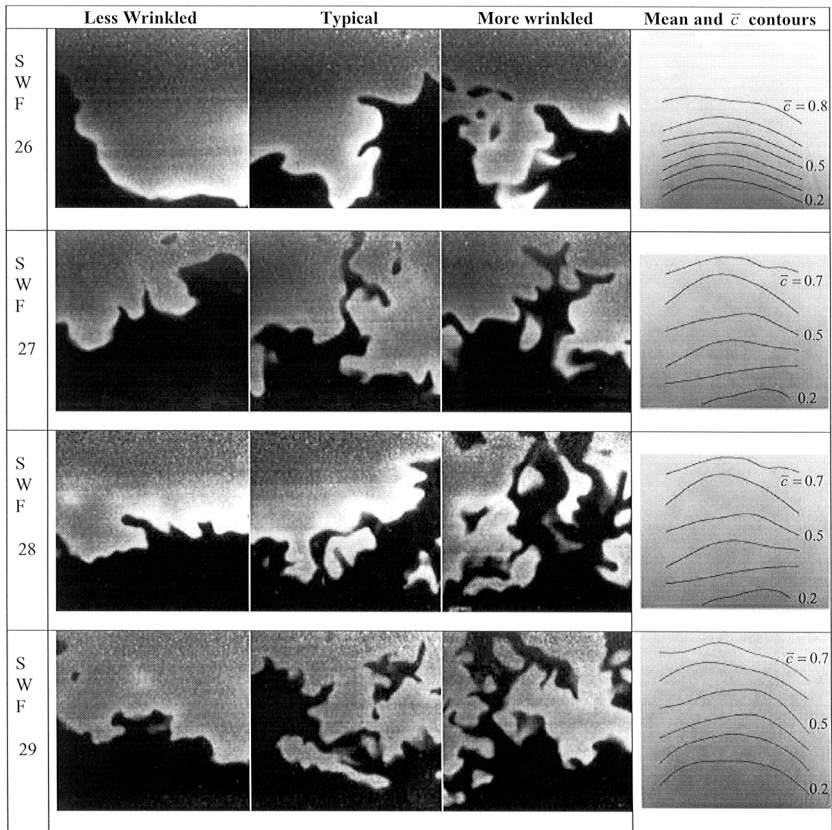


Figure 10. Individual OH-PLIF images obtained for SWF26–29 showing different degrees of wrinkling and their composite images.

thickness, typically from $0.1 < \bar{c} < 0.8$. The \bar{c} contours show all flame brushes to have a slightly inverted bow shape. This overall feature is also found for SWF22–25 (Bedat & Cheng, 1995).

For SWF26 shown at the top row, the flame with the lowest turbulence in this data group, the flame front can be very smooth and has only slight wrinkling (left). At most instances, the flame is more wrinkled with flame cusps (center). There are occasions when the flame is much more wrinkled and forms flame pockets (right). This random behavior is found in all the other flames. The only difference is a change in the degree of flame wrinkling and their features. At the highest turbulence investigated (SWF29), the flame front is more fragmented and forms pockets in both reactants and products. The formation of flame cusps is also rare. These changes are consistent with the skewness of the flame crossing frequency profiles in Figure 8.

These OH-PLIF images clearly demonstrate that flame wrinkling is a random process that requires statistical analysis of sizable data sets. This randomness has been identified and analyzed in a previous study of the fractal dimension for a v-flames in low turbulence (Shepherd & Cheng, 1992). The present set of data provides more supporting evidence of the statistical behavior and shows that high turbulence intensity augments the degree of randomness. Due to this random process, flame wrinkles at a given instance correspond only to a limited range of scales within the full turbulence spectrum. The three columns of Figure 10 may be interpreted as the instances during which the flames interact with turbulence scales in the low (less wrinkled), middle (typical wrinkles), and high (more wrinkled) ranges of the energy spectrum. The important implication for our investigation is that the penetration of small intense vortex into flame sheet may be statistically an extremely rare event.

As mentioned above, exceeding the Klimov-Williams criterion is often used as a criterion for predicting the existence of significant flame front broadening. To investigate the statistical distribution of the OH gradient as a function of Ka , a detailed analysis was performed for two flame images from the lowest and highest u'/S_L cases (SWF26 and SWF29). The images analyzed are shown as insets in Figures 11(a) and 11(b). For each flame the position of the half height of the OH profile at the flame front was obtained by an edge-finding technique. Normals, n , to this line were determined at 1 mm intervals along the line, and the flame front thickness, defined in terms of the maximum gradient, $(d[OH]/dn)_{\max}$, was calculated from the OH profiles along these normals. By this means

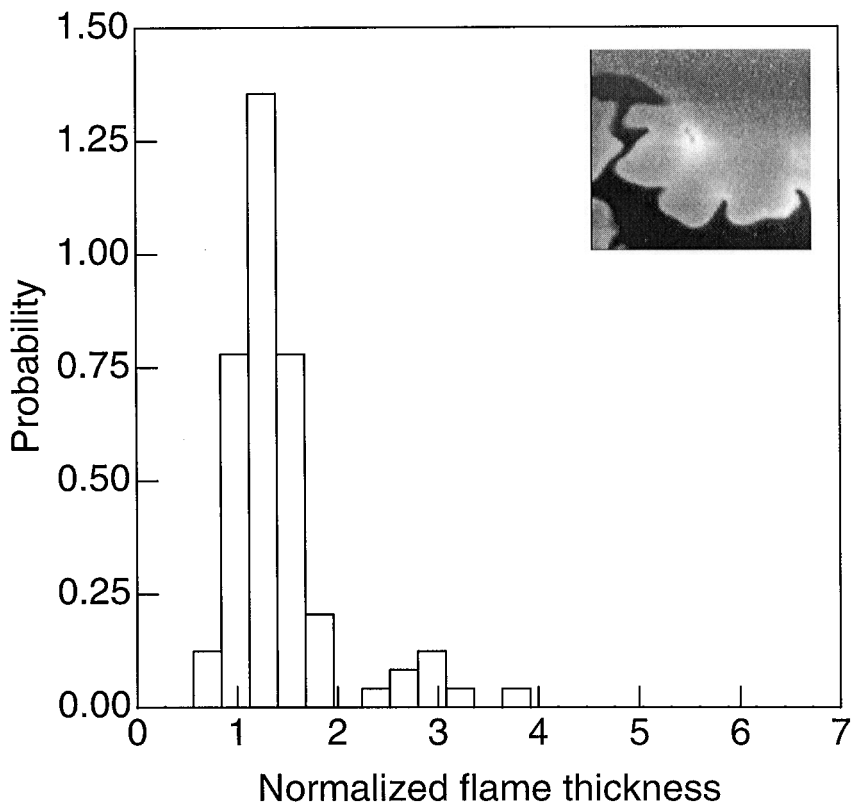


Figure 11(a). Distribution of local flame front thickness, SWF26.

the affect of flame front orientation in the measurement plane could be eliminated. The pdf of flame front thickness, normalized by the laminar value (0.705 mm) are presented in Figures 11(a) and (b). As expected, the laminar value, obtained from a similar OH-PLIF measurement in a laminar conical flame, marks an approximate lower limit to the flame thickness. It is of interest to note here that SWF26 and SWF29 span the Klimov-Williams criterion, $Ka = 0.29$ and 2.73 , respectively, see Figure 1. In the lower turbulence case, SWF26, the “flame front broadening” will not be due to “distributed reaction zones” but rather to out-of-plane flame front orientation effects. There is, however, very little difference in the two distributions and so similar conclusions should apply to SWF29 indicating that a distributed reaction zone interpretation of the Klimov-Williams criterion is not appropriate here. It should be noted that this

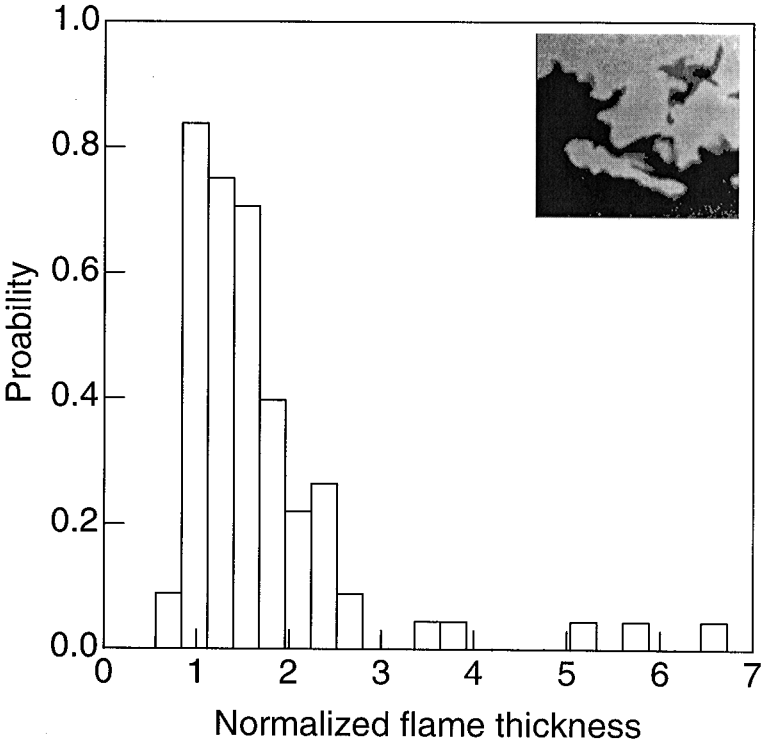


Figure 11(b). Distribution of local flame front thickness, SWF29.

criterion simply marks the boundary where the smallest turbulence scale is equal to the flame scale. Considering the probabilistic nature of turbulence, a more appropriate interpretation would be that the distributed reaction zone regime of $Ka > 1$ represents the conditions under which the probability for small intense eddies to penetrate the flame front is finite. These are sufficient but not necessary conditions for reaction zone broadening to occur as these results demonstrate. It is also of interest to note that there is no correlation between flame front thickness and curvature. Cross-correlation of the local curvature gives very low correlation coefficients of -0.1 and 0.03 for SWF26 and SWF29, respectively. Given the relatively small data sets (~ 90) these are not significantly different.

Analyzing the wrinkled flame front boundaries is a useful means to further illustrate the randomness of flame wrinkling process and to quantify the low probability of small flame wrinkles. For each flame

image, normalized to account for the variations in the intensity of the laser beam profile, the flame front was outlined by an edge-finding algorithm. A threshold value was chosen to mark the steepest gradient in the OH signal. Due to the decrease in OH concentration behind the flame front as it approaches equilibrium values, each edge detected was inspected to ensure that the gradient is comparable to that of a flame front. The gradient is very steep and so the flame front position derived by this method is not very sensitive to the threshold value. From these flame fronts binary images of burned and unburned regions were generated and summed to obtain \bar{c} map of the flame brush (see Figure 10).

A more detailed picture of the effects of increased turbulence on flame wrinkle scales was obtained by analyzing the distribution of the mean local flame front curvatures. The flame edges derived from the PLIF images are smoothed by simple 3×3 averaging to remove digitization noise. Then each point on the flame fronts is fitted with two (for the two coordinates, x and y) third-order polynomials using the distance along the flame edge as the independent variable. The curvature is sensitive to the number of points in the fit and, after some experimentation, a fit performed over 1 mm along the flame edge, i.e., 13 points for all the flame cases, was found to be satisfactory. A third-order fit is used so that inflection points along the flame edge could be accommodated. At each point along the flame edge the local curvature, h_{xy} , is obtained from the fits by the osculator relationship:

$$h_{xy} = (\dot{x}\ddot{y} - \dot{y}\ddot{x})/(\dot{x}^2 + \dot{y}^2)^{1.5}$$

where dot and double dot superscripts to x and y refer to first and second derivatives with respect to distance along the flame edge at the point of interest. By averaging these curvatures the mean positive $+\bar{h}$ and negative $-\bar{h}$ curvatures for each flame image are calculated. From each flame the two sets of mean curvatures data are used to generate separate ensemble averages $+\langle\bar{h}\rangle$ and $-\langle\bar{h}\rangle$ as well as their probability distributions. The total length of the flame edges in each PLIF image varies considerably. So to give the mean curvature calculated from each image equal statistical significance, the flame length determined for that image, \bar{L} , is used to weight the individual contributions to the mean curvature pdfs.

The ensemble averages $+\langle\bar{h}\rangle$ and $-\langle\bar{h}\rangle$ are given in Table 2 with the standard deviations shown in parenthesis. The effect of increased turbulence is immediately apparent: Both $+\langle\bar{h}\rangle$ and $-\langle\bar{h}\rangle$ increase showing that the increase in turbulent kinetic energy at smaller scales (see the corresponding decrease in Kolmogorov scale, l_k , in Table 2) generates

Table 2. Mean flame lengths and curvatures

	l_k mm	$\langle L \rangle$ mm	$-\langle \bar{h} \rangle$ mm ⁻¹	$+\langle \bar{h} \rangle$ mm ⁻¹
SWF26	0.15	104 (35)	-0.200 (0.013)	0.180 (0.006)
SWF27	0.1	132 (40)	-0.236 (0.012)	0.244 (0.008)
SWF28	0.07	158 (49)	-0.266 (0.018)	0.274 (0.013)
SWF29	0.06	165 (52)	-0.270 (0.018)	0.301 (0.016)

a larger mean curvature of the flame fronts. It will be recalled that the turbulence field is almost isotropic with an integral scale of 15 mm for all the cases. The standard deviations of these distributions show a general increase with increasing turbulence, although this affect is more obvious in the positive curvature cases. The distributions for $+\bar{h}$ and $-\bar{h}$ are shown in Figure 12. At first glance, the obvious change is the shifting of their modal values to higher curvatures corresponding to the increases in $+\langle \bar{h} \rangle$ and $-\langle \bar{h} \rangle$. There are, however, subtle changes towards the larger curvature ranges where the pdfs of SWF28 and SWF29 have small but significant contributions. These contributions represent the instances with small scale flame wrinkles when the flame front become convoluted and fragmented. The low probability of these instances provides support to our argument that the influence of small scale turbulence on the flame fronts is indeed a statistically rare event.

For each image, the total length of flame fronts, L , including contributions from the flame pockets, provides a two-dimensional estimate of the instantaneous flame surface area. Ensemble mean values of the flame lengths, $\langle L \rangle$, and the standard deviations are given for SWF26–29 in Table 2. The probability density functions of L obtained from 200 images are shown in Figure 13. From Table 2, $\langle L \rangle$ shows a 60 percent increase from the lowest to highest turbulence levels. This consistent increase in flame length with increasing turbulence intensity is accompanied by a broadening of the pdfs toward the large L values, see, for example, the pdfs in Figure 13 for SWF28 and SWF29. The statistics of L again illustrate the random character of these flame surfaces with large variations in flame length from shot to shot.

In all cases investigated here the integral length scale, l_x , is the same, 15 mm, and the equivalence ratio is also constant, $\phi = 0.7$. These results, therefore, highlight the affects of the increased intensity of the turbulence field and the widening of the turbulence spectrum to smaller scales on mean flame length. The importance of the smaller scales in controlling

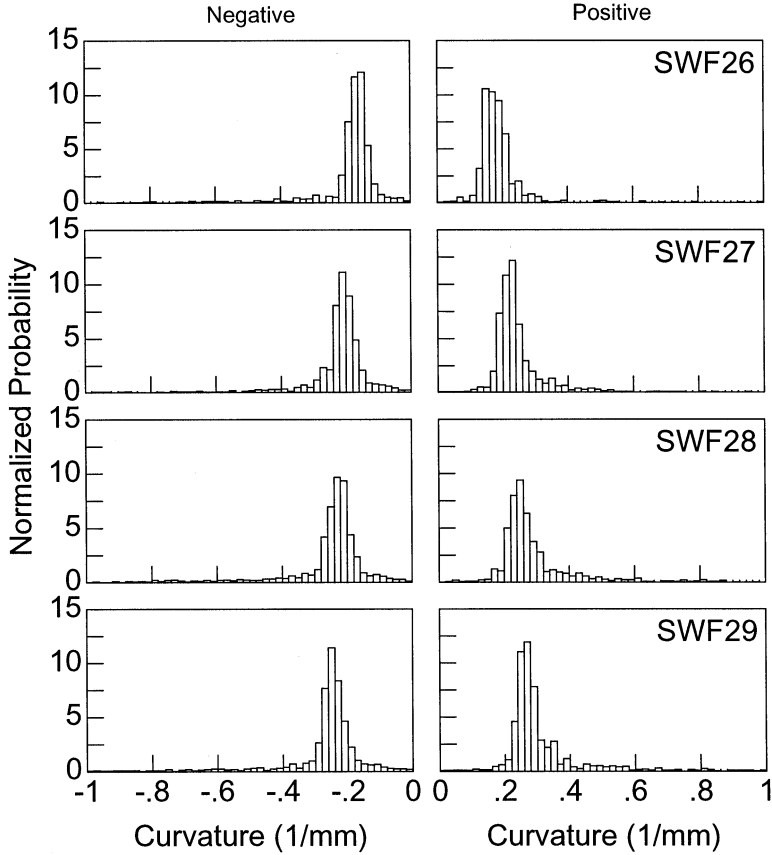


Figure 12. Probability density functions of positive and negative flame curvatures deduced from OH-PLIF images.

the flame length is illustrated in Figure 14 where $\langle L \rangle$ shows an inverse relationship to the Kolmogorov scale, l_k . Bearing in mind the scaling law underlying the value determined for the Kolmogorov scale, this indicates that $\langle L \rangle \propto \text{Re}_t^{-3/4}$.

To infer if the experimentally determined values of $\langle L \rangle$ can be related to the increase in flame surface area, the parameter $(\langle L \rangle / L_{\text{ref}})^2$ is deduced for the four flames and plotted against u' / S_L in Figure 15. Here, L_{ref} is a reference length and is taken to be the width of the OH-PLIF image (40 mm). $(\langle L \rangle / L_{\text{ref}})^2$ is then an effective increase in flame

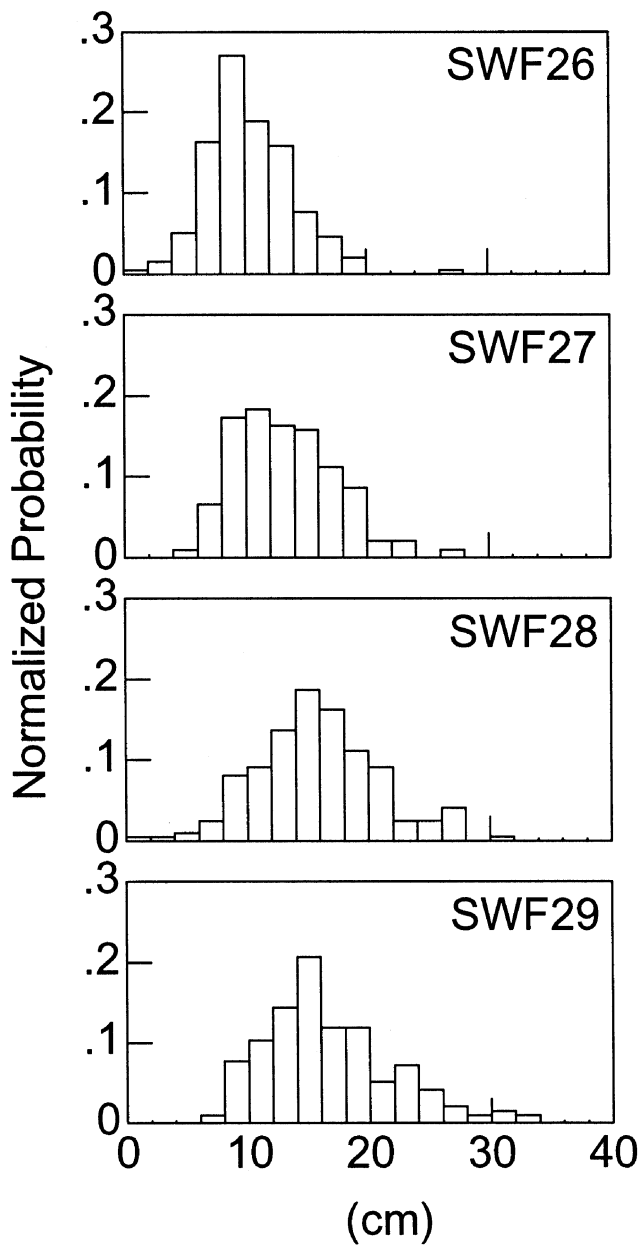


Figure 13. Probability density functions of flame length deduced from OH-PLIF images.

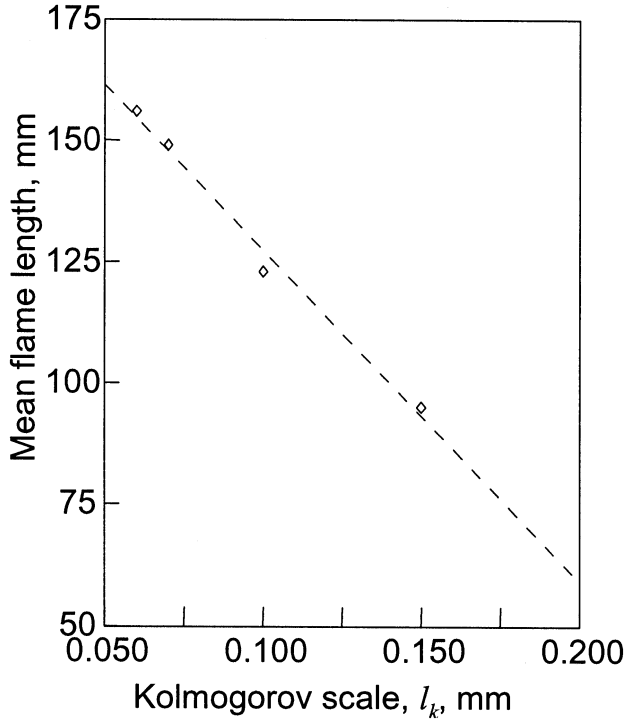


Figure 14. Mean flame lengths determined from PLIF images.

surface area. For an idealized 1-D flame, it should be identical to S_f/S_L and increase linearly with u'/S_L . As seen in Figure 15, a linear relationship for $(\langle L \rangle/L_{\text{ref}})^2$ and u'/S_L exists. However, with the exception of SWF26, all the values are lower than S_f/S_L . As a reference, the linear correlation of S_f/S_L is also plotted in Figure 15. It can be seen that the linear fit of the $(\langle L \rangle/L_{\text{ref}})^2$ data has a lower slope than the S_f/S_L correlation. Despite these difference, the results shown here are encouraging and will be a useful reference for the analysis of the flame surface density from the OH-PLIF images.

CONCLUSIONS

Laser schlieren, laser tomography, and planar laser induced fluorescence for OH (OH-PLIF) techniques have been used to investigate pre-mixed turbulent flame structures under moderate to intense isotropic

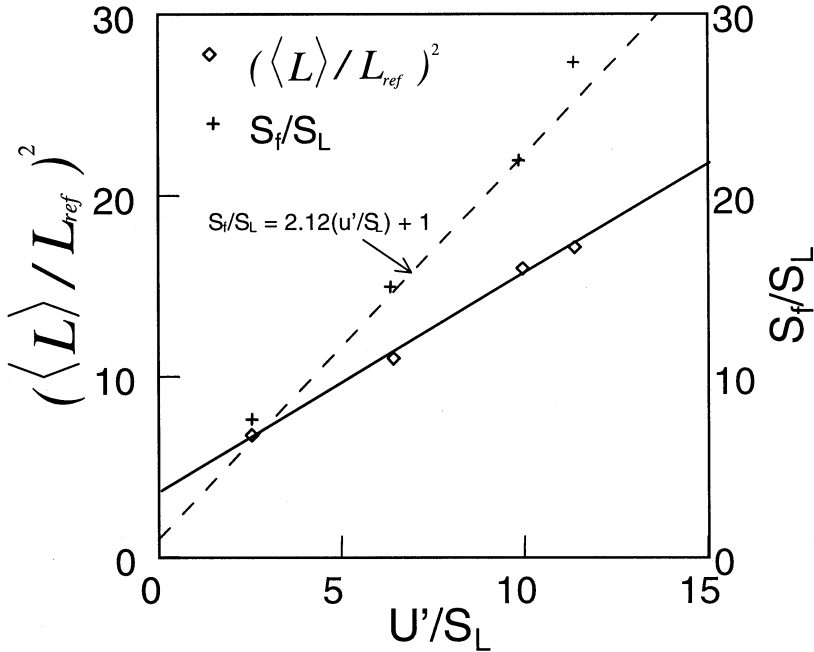


Figure 15. Flame area ratio estimated from flame lengths compared to flame speed correlation.

turbulence. The goal is to gain better insights into the flame structures at high turbulence and to test and verify the concept of the distributed reaction zones regime. Unconditioned velocity statistics were measured using a two-component laser Doppler anemometry system. The experiments were conducted using a low-swirl burner fitted with a turbulence generator that produces high intensity, near-isotropic turbulence.

Four methane/air flames with the same equivalence ratio ($\phi = 0.7$) have been studied. By increasing the total flow rate from 5 to 20 L/s, the rms velocity was varied from 0.5 to 2.2 m/s. All flames were stabilized at swirl number $S = 0.1$. The velocity data show that under high turbulence and lean conditions the flames do not generate significant flow acceleration or experience increases in unconditioned rms velocities. The turbulent flame speeds, S_f , deduced for the four flames together with those obtained previously in our other low-swirl burner studies were correlated with the rms velocity, u' . The set of data show linear correlation of $S_f/S_L = 2.12 (u'/S_L) + 1$ but not the nonlinearity reported for other premixed turbulent flame configurations.

The schlieren images demonstrated that this line-of-sight flow visualization technique is not suitable for investigating flame structures. The MSOD tomographic images show greater details of the flame wrinkles and its large field of view (100×100 mm) is convenient for observing overall flame behavior. The aerosol droplet density, however, was found to be a limitation because it was not sufficiently high to resolve the small flame wrinkled structures. Although the field of view of our OH-PLIF system is smaller (40×40 mm), it captures most of the flame brush and resolves the fine wrinkle structures.

The set of 200 OH-PLIF images obtained for each of the four flames clearly shows that flame wrinkling is a random process that requires statistical analysis of a sizable data set. Due to this randomness, flame wrinkles at a given instance display only a limited range of turbulence scales. The probability of the flame showing the smallest wrinkles is relatively low. The important implication is that the penetration of small intense eddies into the flame sheet may be statistically an extremely rare event. Therefore, the distributed reaction zone regime of $Ka > 1$ should be interpreted as the regime where the probability for small intense turbulence to penetrate the flame sheet is finite. This interpretation is consistent with recent numerical and theoretical results suggesting that the flamelets are resilient to penetration by small eddies.

The OH-PLIF images were processed to determine statistical properties of the mean flame curvatures and flame lengths for comparison with turbulence intensity and turbulent length scales. The results show that the increase in turbulent kinetic energy at smaller scales (corresponding to a decrease in Kolmogorov scale) generates larger mean curvature of the flame fronts. Low probability of instances with large mean flame curvatures supports the argument that the influence of the smallest turbulence eddies on the flame fronts is a rare event. The mean flame length scales inversely with the Kolmogorov scale. An estimate of the increase in flame area ratio with turbulence shows a linear relationship but the rate of increase is lower than that of the flame speed ratio.

NOMENCLATURE

Flow Parameters

U, u'	mean and rms axial velocities (m/s)
V, v'	mean and rms radial velocities (m/s)

W, w'	mean and rms circumferential velocities (m/s)
l_x	integral length scale (mm)
l_k	Kolmogorov scale
a_b	mean aerodynamic stretch $= dU/dx$ (sec^{-1})
a_T	turbulent stretch $\equiv u'/l_x$ (sec^{-1})
Q	volumetric flow rate of premixture (litre/sec)
S	swirl number $= \frac{\pi r_0 R}{A_t} \left(\frac{m_\theta}{m_\theta + m_A} \right)$; r_0 , radius of the swirl jets; R, burner radius; A_t , total area swirl air jets; m_θ tangential mass flow rate; m_A axial mass flow rates.

Flame Parameters

ϕ	equivalence ratio
ρ	density
τ	density ratio $= \rho_r/\rho_p - 1$
\bar{c}	progress variable $= (\bar{p} - \rho_0)/(\rho_r - \rho_0)$
d_L	reaction zone thickness
Da	Damkohler number $= (l_x/d_L)(u'/S_L)^{-1}$
D_f	turbulent flame brush thickness
f	flame crossing frequency, sec^{-1}
$+\langle \bar{h} \rangle$	mean positive flame curvature (convex to the reactants)
$-\langle \bar{h} \rangle$	mean negative flame curvature (concave to the reactants)
Ka	Karlovitz number $= (u'/S_L)^{3/2} (l_x/d_L)^{-1/2}$
—	mean flame length determined from an OH-PLIF image
$\langle l_T \rangle$	averaged flame length determined from a set of OH-PLIF images
S_L	laminar flame speed
S_f	turbulent flame speed
ΔU	relative velocity $\equiv U_p - U_r$
Δu_L	relative velocity of a normal 1-D laminar flame $= S_l(\tau - 1)$
Σ	flame area per unit volume
v	flame crossing frequency
K_t	indicator parameter for the effects of flames on turbulence, $(a_t + a_b)/\Delta u_L$ (m^{-1})
K_F	extinction criterion $= 2a_b/\Delta u_L$

Subscripts

L	laminar condition
-----	-------------------

T	turbulent condition
p	conditioned products properties
r	conditioned reactants properties
∞	reference flow conditions without swirl

REFERENCES

- Bedat, B. and Cheng, R.K. (1995) Experimental study of premixed flames in intense isotropic turbulence. *Combust. and Flame*, **100**, 485–494.
- Bedat, B. and Cheng, R.K. (1996) Effects of buoyancy on premixed flame stabilization. *Combust. and Flame*, **107**, 13–26.
- Borghì, R. (1985) In F. Casei, ed., *Recent Advances in the Aerospace Sciences*, Plenum Press, New York. pp. 117–138.
- Bradley, D. (1992) How fast can we burn. *Proc. Comb. Inst.*, **24**, 279–285.
- Bray, K.N.C. (1990) Studies of the turbulent burning velocity. *Proceedings of the Royal Society of London A*, **431**, 315–335.
- Chan, C.K., Lau, K.S., Chin, W.K., and Cheng, R.K. (1992) *Proc. Comb. Inst.*, **24**, 519–525.
- Cheng, R.K. (1995) Velocity and scalar characteristics of premixed turbulent flames stabilized by weak swirl. *Combust. and Flame*, **101**, 1–14.
- Claypole, T.C. and Syred, N. (1980) *Proc. Comb. Inst.*, **18**, 81–89.
- Damköhler, G. (1940) The effects of turbulence on the flame velocity in gas mixtures. *Elektrochem.*, **46**, 601.
- Furukawa, J., Harada, E., and Hirano, T. (1990) *Proc. Comb. Inst.*, **23**, 789–794.
- Jarosinski, J. (1984) Brief communications: The thickness of laminar flames, *Combust. and Flame*, **56**, 337–342.
- Peters, N. (1986) Laminar flamelet concepts in turbulent combustion. *Proc. Comb. Inst.*, **21**, 1231–1250.
- Peters, N. (1998) Propagating thin reaction zones in premixed turbulent combustion, Part I: Theory and modeling aspects. Private communication.
- Poinsot, T., Veynante, D., and Candel, S. (1990) Diagrams of premixed turbulent combustion based on direct simulation. *Proc. Comb. Inst.*, **23**, 613–619.
- Pope, S.B. and Anand, M.S. (1984) Flamelet and distributed combustion in premixed turbulent flames. *Proc. Comb. Inst.*, **20**, 403–410.
- Shepherd, I.G., Cheng, R.K., and Talbot, L. (1992) Experimental Criteria for the Determinates of Fractal Parameters of Premixed Turbulent Flames, *Exp. in Fluids*, **13**, 386–392.
- Taylor, S.C. (1991) Ph.D. Diss., University of Leeds, Leeds, UK.
- Tseng, L.K., Ismail, M.A., and Faeth, G.M. (1993) Laminar burning velocities and Markstein numbers of hydrocarbon/air flames. *Combust. and Flame*, **95**, 410–426.

- Videto, B.D. and Santavicca, D.A. (1991) A turbulent flow system for studying turbulent combustion processes. *Combust. Science and Technology*, **76**, 159–164.
- Williams, F.A. (1985) *Combustion Theory (2nd ed.)*. Addison-Wesley, Reading, MA. p. 680.
- Yoshida, A., Narisawa, M., and Tsuji, H. (1992) *Proc. Comb. Inst.*, **24**, 527–535.